Terrain Modelling from lidar range data in natural landscapes: a predictive and Bayesian framework

Frédéric Bretar, Nesrine Chehata

Elsevier Editorial System(tm) for Computer Vision and Image Understanding
Manuscript Draft

Manuscript Number:

Title: Terrain Modelling from lidar range data in natural landscapes: a predictive and Bayesian framework

Article Type: Special Issue: New Advances/3D Imaging

Section/Category:

Keywords: Lidar data; Terrain Digital Model; Predictive filter; Markovian regularization; 3D point cloud

Corresponding Author: Dr Frederic Bretar, Ph.D.

Corresponding Author's Institution: IGN

First Author: frederic bretar, PhD

Order of Authors: frederic bretar, PhD; Chehata Nesrine, PhD

Manuscript Region of Origin:

Abstract: The Earth's topography, including vegetation and human-made features, reduced to a virtual 3D representation is a key geographic layer for any extended development or risk management project. Processed from multiple aerial images, or from airborne lidar systems, the 3D topography is first represented as a point cloud. This article deals with the generation of Digital Terrain Models in natural landscapes.

We present a global methodology for estimating the terrain height by deriving a predictive filter paradigm. Under the assumption that the terrain topography (elevation and slope) is regular in a neighbouring system, a predictive filter combines linearly the predicted topographic values and the effective measured values. In this paper, it is applied to 3D lidar data which are known to be of high altimetric accuracy. The algorithm generates an adaptive local geometry wherein the altimetric distribution of the point cloud is analysed. Since local terrain elevations depend on the local slope, a predictive filter is first applied on the slopes then on the terrain elevations. The algorithm propagates through the point cloud following specific rules in order to optimize the probability of computing areas containing terrain points. Considered as an initial surface, the

previous DTM is finally regularized in a Bayesian framework. Our approach is based on the definition of an energy function that manages the evolution of a terrain surface. The energy is designed as a compromise between a data attraction term and a regularization term. The minimum of this energy corresponds to the final terrain surface. The methodology is discussed and some conclusive results are presented on vegetated mountainous areas.

Dear Editor-in-Chief,

The article **"Terrain Modelling from lidar range data in natural landscapes: a predictive and Bayesian framework"** is submitted to the Special Issue: New advances in 3D-imaging and modelling. I have submitted it in due time (May 2008), unfortunatly, some troubles on the website concerning this submission appeared. By chance, I have visited the website on friday Septembre, 5th and saw that the review process has not begun yet. Since May 2008, I have not had any feed back (email) from the journal.

This study deals with the generation of 3D terrain surfaces (digital elevation models) based on 3D lidar points. A 3D point cloud represents the whole topography including ground, off-ground points and also negative or positive outliers. The algorithm is based on two steps. First, a filtering process based on the both adaptation of the local neighboring environment (presence of vegetation, slope). Secondly, a regularization process leads to a fine terrain surface that handles discontinuities and steep relieves.

The paper presents aerial lidar sensors that provide accurate 3D point clouds of topography. A complete metholodology is presented for handling 3D-data from filtering process to fine surface production. Our interest was focused on mountaineous vegetated areas wich present a complex topography with mountains peaks, talwegs, discontinuities and microrelieves. The process is operational on large data sets with complex topography.

Terrain Modelling from lidar range data in natural landscapes: a predictive and Bayesian framework

Frédéric Bretar [a,*] ,Nesrine Chehata [b]

[a] *Institut Géographique National,*

Laboratoire MATIS,

4 Av. Pasteur, 94165 St. Mandé cedex, France

[b] *Institut EGID - Université Bordeaux 3*

1 Allée Daguin 33607 Pessac, France

Email: Nesrine.Chehata@egid.u-bordeaux3.fr

Abstract

The Earth's topography, including vegetation and human-made features, reduced to a virtual 3D representation is a key geographic layer for any extended development or risk management project. Processed from multiple aerial images, or from airborne lidar systems, the 3D topography is first represented as a point cloud. This article deals with the generation of Digital Terrain Models in natural landscapes. We present a global methodology for estimating the terrain height by deriving a predictive filter paradigm. Under the assumption that the terrain topography (elevation and slope) is regular in a neighbouring system, a predictive filter combines linearly the predicted topographic values and the effective measured values. In this paper, it is applied to 3D lidar data which are known to be of high altimetric accuracy. The algorithm generates an adaptive local geometry wherein the altimetric distribution of the point cloud is analysed. Since local terrain elevations depend on the local slope, a predictive filter is first applied on the slopes then on the terrain elevations. The algorithm propagates through the point cloud following specific rules in order to optimize the

probability of computing areas containing terrain points. Considered as an initial surface, the previous DTM is finally regularized in a Bayesian framework. Our approach is based on the definition of an energy function that manages the evolution of a terrain surface. The energy is designed as a compromise between a data attraction term and a regularization term. The minimum of this energy corresponds to the final terrain surface. The methodology is discussed and some conclusive results are presented on vegetated mountainous areas.

---

* Corresponding author

email: Frederic.Bretar@ign.fr

1 Introduction

Representing the Earth's topography, that is the vegetation, the true terrain, buildings as well as any human-made infrastructures from aerial remote sensors in a 3D virtual environment has been a challenging task for scientists for many years. A Digital Terrain Model (DTM) is a fundamental layer for any application in a 3D virtual environment, and as a matter of course, plays a main role when dealing with natural risk management. The 3D cartography of flooding zones, the 3D simulation of polluted fluids or any electromagnetic propagation fields are as much as relevant applications which rely on the accurate geometry of virtual scenes in general, and particularly on the quality of a DTM.

In the context of aerial survey, images acquired in a multi-stereoscopic configuration can be used to derive 3D information of the surface using correlation techniques [1]. However, these techniques fail when radiometric inhomogeneities appear between stereoscopic couples or when textural information are not discriminant enough. Furthermore, the terrain cannot be directly estimated when it is occluded by vegetation.

Airborne laser systems may sort out these problems under certain conditions. They are based on the recording of the time-of-flight distance between an emitted laser pulse and its response after a reflection on the ground. They provide sets of tridimensional irregularly distributed points, georeferenced with an integrated GPS/INS system within an altimetric precision less than 0.1 m [2]. Moreover, these systems can provide multiple returns for a single laser pulse which correspond to different encountered obstacles. It is particularly relevant when surveying vegetated areas where the altitude of the canopy top, intermediate points and even the ground can

be recorded at once with accuracy. Nevertheless, dense vegetation inhibits laser ground return signal. The aim of this paper is to present a full methodology for generating DTMs from airborne 3D lidar data. Once the DTM calculated, lidar points near the terrain surface can be classificated as ground points. Sithole [3] did perform a detailed review and qualification of classification algorithms generally used when processing lidar data. Three main approaches have been developed in the literature and will be briefly described hereafter.

(1) the **morphological** approach is based on series of morphological openings and closings on the 3D point cloud [4]. A dual-rank filter has also been used to manage DTM generation [5], with an evolution of the structural element size [6].
(2) the **iterative Triangular Irregular Network generation** approach that consists, from a coarse triangulated surface based on the lowest points, in integrating new lidar points in a Delaunay triangulation under strong angle and distance constraints [7].
(3) a **modified kriging** approach [8]. It consists in modifying the interpolator parameters depending on a weighting function associated to lidar points. Weights are a combination of variance-covariance values which are modelled as a power function of the residuals between the interpolated terrain value and the elevation of lidar points. The surface converges towards points with negative residuals.

If the described approaches are highly parametrizable (that make them flexible), we aim at providing a system with very few parameters. Our approach is based on the local observation of lidar points by identifying those that belong to the terrain surface. It consists in the integration of three concepts used independently in the

previous approaches: Firstly, lowest lidar points in a defined neighbourhood have a higher probability of belonging to the terrain than the others. Secondly, since the terrain surface may have been occluded either by the vegetation or by buildings, it appears to be necessary to adapt the local neighbourhood in order to ensure terrain points to belong to it. Finally, we assume most of terrain surfaces to be locally regular.

In this paper, we present an original and general methodology for generating DTMs from altimetric data. It is applied to 3D lidar data. Section 2 is dedicated to the management of the point cloud. We describe the topology (section 2.1), the propagation rules within the data sets (section 2.2) as well as the adaptive neighbourhood strategy (section 2.3). We introduce in section 3.1 the general framework of the predictive filter paradigm for DTM estimation. The integration of the local slope in this framework is highlighted and discussed in section 3.2. We propose then to derive the paradigm for calculating the terrain height in section 3.3. The assumption of the terrain surface to be regular provides low spatial frequencies of the true terrain. Or, lidar points are meant to describe relevant micro-relieves for any pre-cited application within a 0.1 m alyimetric accuracy. We therefore introduced in our system a regularization step (section 4) which integrates lidar points near the terrain surface. Considered as an initial surface, the DTM is regularized in a Bayesian framework. Finally, the methodology is discussed in light of some results and future works are proposed in section 5.

2 Pre-processing and data management

2.1 Topology

A lidar survey is made of numerous binary files, either representing entire strips or subsets of numerous strips as a paving decomposition (figure 1). Indeed, a lidar survey is generally composed of several millions of 3D points. It depends on the area of the survey and on the point density. A subset of lidar points is therefore represented as sets of binary files containing various attributes. Among them, there are the x,y,z geographic coordinates, the lidar intensity in the near Infra-Red domain. After the processing, other attributes can be added such as classification label (e.g. ground, off-ground, vegetation, buildings ...) or the normal vector information. Since we are dealing with topographic surfaces (2.5D), the point cloud topology is managed with a quadtree structure. In the following, requests on the quadtree are cylinder neighbouring extractions of various diameters $\mathbf{d}_s$. We denote $\mathcal{V}_s$ such neighborhood, s representing the corresponding image site (pixel) on the future DTM, (s_x, s_y) the related coordinates in the 3D space.

$$\mathcal{V}_s = \{l \in \text{point cloud} / (s_x - l_x)^2 + (s_y - l_y)^2 \leq (\mathbf{d}_s/2)^2, \mathbf{d}_s \in \mathbb{R}^+\} \qquad (1)$$

2.2 Propagation rules

The system is designed to generate a DTM in a (planimetric) 2D development strategy through the lidar point cloud. Considering the DTM as a georeferenced regular gridded surface or as a set of sites s (pixels), the system explores the lidar point cloud following this gridded geometry. The propagation strategy is designed to en-

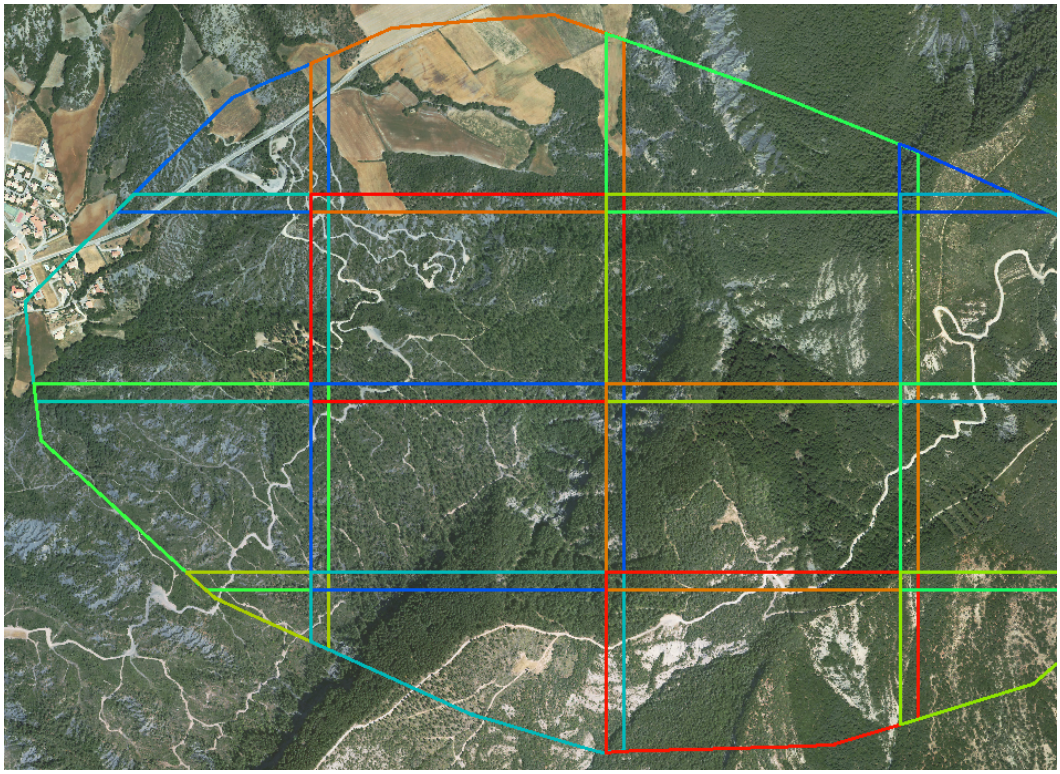

Fig. 1. Display of a paved lidar survey over a mountainous area. The background image is an orthorectified image from IGN®.

sure that sites containing terrain points will be processed before those containing only off-ground points so that the coherence of terrain measurements should be optimized. As a result, the system explores the point cloud following the gridded site topology in the native image neighbouring system (4/8-connectivity). For each visited site s (see black sites on figure 2), neighbouring sites are extracted (extruded sites on figure 2). On figure 2, extruded sites describe the frontier set of the propagation. Each site of the frontier is valued to the altimetric variance of a subset of lidar points included in $\mathcal{V}_s$. Here, the diameter $\mathbf{d}_s$ of $\mathcal{V}_s$ is set so that at least 10 lidar points should belong to the neighbourhood. The altimetric variance is calculated over the 20% lowest points to minimize the dispersion due to off-ground points. Finally, the system propagates towards the site with the lowest variance among the frontier set. Note that the propagation strategy is independent of the DTM calcula-

tion.

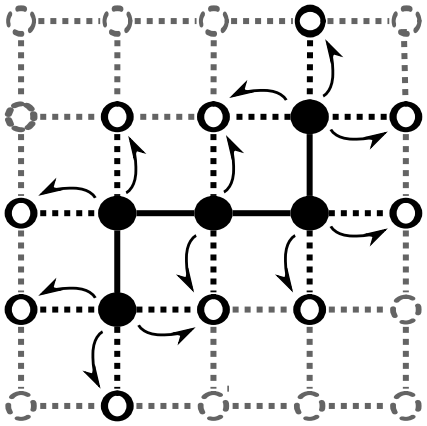

Fig. 2. Set of DTM sites. The system propagates towards the site with the lowest variance among the frontier sites (extruded circles) in a 4-connectivity topology.

2.3 Adapting the local neighbouring system

Depending both on the geometrical and optical properties of topographic objects, a lidar pulse may or may not penetrate off-ground objects. In case of opaque human-made features like buildings, only one return pulse corresponds to an emitted lidar pulse. However, in case of vegetated areas, an incident lidar pulse will interact with the canopy and be returned as a complex shape. It will be seen as multiple echo returns by the sensor. Mainly depending on the leaf density, a lidar measurement will be composed of several echos: the last recorded one (farthest from the sensor) may describe the true terrain.

Processing a DTM from lidar data consists in recognizing 3D points that belong to the terrain from those not. In our approach, it comes to explore the 3D local environment ($\mathcal{V}_s$) of each DTM site and to calculate the terrain height from the lidar point cloud (cf. section 3.1). In case of bare Earth landscapes, the smaller the diameter of $\mathcal{V}_s$, the more realistic the estimation of the ground: there is a limited smoothing ef-

fect. However, when processing natural landscapes with vegetation, the higher the altimetric variance of lidar points within $\mathcal{V}_s$, the weaker the probability for lower points to belong to the true terrain. As a result, increasing the neighbouring size $\mathbf{d}_s$ with the altimetric variance and/or with prior knowledge of the landscape will increase the probability of finding ground lidar points in $\mathcal{V}_s$.

We therefore propose to include prior knowledge related to off-ground objects in the calculation of the neighbourhood size (here, the diameter of the cylinder, eq. 1) as an off-ground mask $\mathcal{M}$ [9]. It is a binary image of DTM like resolution. We are focusing the DTM calculation on natural areas composed of vegetated and bare Earth landscapes. The case of buildings is not treated in this paper, but the same rules can be applied when buildings are detected.

Assuming that the standard deviation σ_s of lidar points belonging to $\mathcal{V}_s$ is greater in case of off-ground features than bare Earth areas, we consider a site s to belong to $\mathcal{M}$ if σ_s is greater than a threshold. This threshold is often set to 1 m.

As mentioned previously, the size $\mathbf{d}_s$ of the cylinder should be small enough to keep all ground details but large enough to ensure the removal of off-ground objects such as trees or/and buildings. The section describes an algorithm for adapting the diameter $\mathbf{d}_s$ of the cylinder at site s to natural areas. The adaptive diameter $\mathbf{d}_s$ is processed over lidar points belonging to $\mathcal{M}$. By definition, if the projection of a lidar point is included in $\mathcal{M}$, it is likely to belong to a vegetated area. $\mathbf{d}_s \in [\mathbf{d}_s^{\min}, \mathbf{d}_s^{\max}]$ should therefore be enlarged to ensure that enough lidar points within $\mathcal{V}_s$ belong to the true terrain.

$\mathbf{d}_s^{\min}$ is a critical parameter and has to be defined so that a minimum number of lidar points should be processed within $\mathcal{V}_s$. Besides, $\mathbf{d}_s^{\min}$ ensures the overlapping

structure of neighbourhoods. We therefore constrain $\mathbf{d}_s$ as:

$$\mathbf{d}_{\text{min}}^{\text{abs}} < \mathbf{d}_s^{\text{min}} \leq \mathbf{d}_s \leq \mathbf{d}_s^{\text{max}} \tag{2}$$

where $\mathbf{d}_{\text{min}}^{\text{abs}}$ is a global minimal diameter over the entire survey and is independent of site s. if r is the DTM ground resolution and $\overline{\delta}$ the global average point density, $\mathbf{d}_{\text{min}}^{\text{abs}}$ is defined as:

$$\mathbf{d}_{\text{min}}^{\text{abs}} = \max(2\sqrt{\frac{10}{\pi * \overline{\delta}}}, 2r) \tag{3}$$

$\mathbf{d}_s^{\text{min}}$ depends on two parameters: i) the trunked standard deviation σ_s^{loc} calculated on the 20% lowest lidar points of $\mathcal{V}_s$ and ii) the neighbouring laser points that belong to $\mathcal{M}$. The higher the local standard deviation σ_s^{loc}, the larger the minimum window size $\mathbf{d}_s^{\text{min}}$. Statistically, low standard deviations of altitudes are over represented in rural areas. Therefore, $\mathbf{d}_s^{\text{min}}$ has to be highly increasing with low values of σ_s^{loc}. We then define the variations of $\mathbf{d}_s^{\text{min}}$ as:

$$\mathbf{d}_s^{\text{min}} = \mathbf{d}_{\text{min}}^{\text{abs}} + c\log(1 + \sigma_s^{loc}); c \in \mathbb{R} \tag{4}$$

$c = 6$ was found to be a good compromise for processing our data. To ensure the regularity of adjacent $\mathbf{d}_s^{\text{min}}$ values, a Gaussian filter is applied over the $\mathbf{d}_s^{\text{min}}$ image provided that equation 2 is still satisfied.

$\mathbf{d}_s^{\text{min}}$ also depends on the set of neighboring sites of s that belong to $\mathcal{M}$. This set is denoted $\{\mathcal{V}_{s\rightarrow\text{DTM}} \bigcap \mathcal{M}\}$ where $\mathcal{V}_{s\rightarrow\text{DTM}}$ is the corresponding sites of $\mathcal{V}_s$ in the DTM topology. We have card $\left(\mathcal{V}_{s\rightarrow DTM} = \text{floor}(\left(\frac{\mathbf{d}_s^{\text{min}}}{r}\right)^2)\right)$. This criteria discriminates small vegetated regions from denser forest areas. From an initial value calculated in equation 4, $\mathbf{d}_s^{\text{min}}$ is increased by one DTM's resolution unit while all neighbouring sites are included in $\mathcal{M}$.

$\mathbf{d}_s^{\text{max}}$ is set proportional to $\mathbf{d}_s^{\text{min}}$. A low value of $\mathbf{d}_s^{\text{min}}$ should correspond to a small

vegetated area and $\mathbf{d}_s$ has therefore to vary in a small interval. On the contrary, a high $\mathbf{d}_s^{\min}$ is likely to correspond to a forest area. To ensure terrain points be statistically represented in $\mathcal{V}_s$, $\mathbf{d}_s$ has to vary within a large interval. We set $\mathbf{d}_s^{\max} = 5\mathbf{d}_s^{\min}$.

For each site s and a neighbourhood diameter $\mathbf{d}_s^{\min}$, let us consider the percentage of predicted off-ground area in $\mathcal{V}_s$:

$$\rho_s = \frac{\text{card}(\mathcal{V}_{s\to DTM} \bigcap \mathcal{M}) r^2}{\pi\left(\frac{\mathbf{d}_s^{\min}}{2}\right)^2} \in [0,1] \tag{5}$$

The behaviour of $\mathbf{d}_s$ between $\mathbf{d}_s^{\min}$ and $\mathbf{d}_s^{\max}$ is not a linear function because the diameter of the cylinder has to be strongly enlarged in case of a high vegetated ratio where lowest points are not guaranteed to belong to the true terrain. Meanwhile, in case of low ratios, one can expect that lowest laser points belong to the true terrain and describe it in details. $\mathbf{d}_s$ will consequently increase exponentially with ρ_s following equation 6.

$$\mathbf{d}_s(\rho_s) = Ae^{\beta\,\rho_s^2} + B \tag{6}$$

With

$$\begin{cases} \mathbf{d}_s(0) = \mathbf{d}_s^{\min} \\ \\ \mathbf{d}_s(1) = \mathbf{d}_s^{\max} \end{cases}$$

we have

$$A = \frac{\mathbf{d}_s^{\max} - \mathbf{d}_s^{\min}}{e^{\beta} - 1} \text{ and } B = \mathbf{d}_s^{\min} - A$$

Parameters in equation 6 were chosen so that $\mathbf{d}_s$ should be highly enlarged when more than half the neighbouring sites of s contains off-ground sites, i.e. when $\rho_s > 0.5$. We therefore choose a ρ_s^2 dependency of the exponential function and $\beta = 3$ for two main grounds (figures 3 and 4):

i. the slope is smaller than a simple exponential when $\rho_s < 0.5$. This ensures a regularized $\mathbf{d}_s$ map that is not sensitive to low vegetated areas.

ii. the slope is higher than a simple exponential when $\rho_s > 0.5$. This ensures a quick increase of the diameter in case of dense vegetated areas.

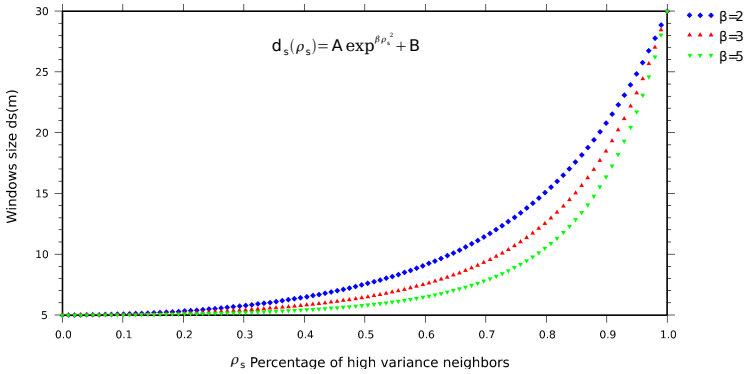

Fig. 3. Comparison of two parametric forms of $\mathbf{d}_s$.

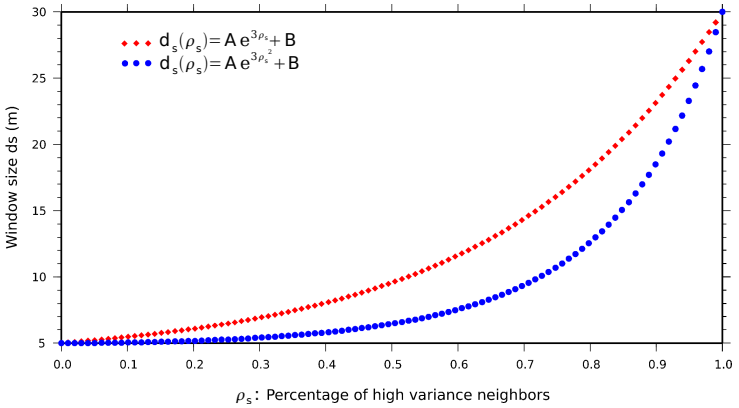

Fig. 4. Variations of $\mathbf{d}_s$ with $\beta \in \{2, 3, 5\}$.

3 A predictive filter for estimating a DTM

3.1 General framework

In its traditional formulation, a predictive filter relates a state prediction of the system at a certain step given the previous state with an effective measurement of the

state vector via their respective uncertainties. The final state value is a linear combination of both the prediction and the measurement [10]. Our system is designed to propagate following a spatial scale (section 2.2). It is represented at a site k as a $n \times 1$ state vector $\mathbf{x}_k = (x_{1,k} \dots x_{n,k})^T$ and a $n \times n$ covariance matrix $\mathbf{S}_k$. It evolves depending on a state relation and a measurement relation.

The state relation considers the transition from a site k given its local environment $\mathbb{V}_k$ (figure 5) to the following site $k+1$ and is represented as a $n \times m$ transition matrix denoted $\mathbf{\Phi}_{\mathbb{V}_k}$. If $\preccurlyeq$ is an ordered relationship along the trajectory of our system, $\mathbb{V}_k = \{s_i / s_i \preccurlyeq k\}_i$ is defined as the set of neighbouring sites s_i (8-connectivity topology) of $k+1$ which have already been visited (see figure 5). We have card$(\mathbb{V}_k) \leq 8$ and $k+1 \notin \mathbb{V}_k$.

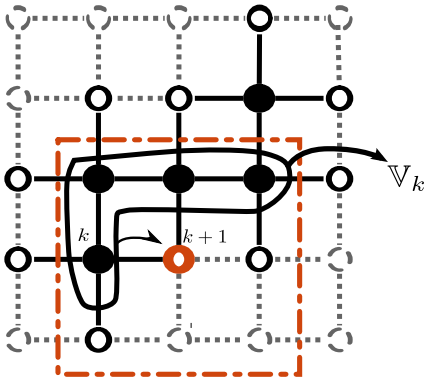

Fig. 5. Definition of $\mathbb{V}_k$. Black sites have already been processed whereas site $k+1$ is the next one to be processed.

Equation 7 (state relation) describes a model of the terrain topography generation seen as a recursive process. Here, we consider that the topography (terrain value and local slope) value at site $k+1$ has a strong correlation with neighbouring sites of $\mathbb{V}_k$. This correlation is translated through the transition matrix $\mathbf{\Phi}_{\mathbb{V}_k}$ as a mean operator on $\mathbb{V}_k$. The state relation can be written as:

$$\mathbf{x}_{k+1|\mathbb{V}_k} = \mathbf{\Phi}_{\mathbb{V}_k} \mathbf{x}_{\mathbb{V}_k} + \mathbf{w}_k \tag{7}$$

where $\mathbf{w}_k$ is a white noise with covariance $\mathbf{Q}_k$ and $\mathbf{x}_{\mathbb{V}_k}$ is a $\max(\text{card}(\mathbb{V}_k), 8) * \dim(\mathbf{x}_k)$ vector with

$$\mathbf{x}_{\mathbb{V}_k} = \left(\underbrace{x_{1,s_1} \dots x_{1,s_8}}_{X_1}, \dots, \underbrace{x_{n,s_1} \dots x_{n,s_8}}_{X_n} \right)^T \tag{8}$$

Let us define the line 1×8 matrix $\Big(\mathbb{1}(X)\Big)_{\mathbb{V}_k}$ where $X \in \{X_1 \dots X_n\}$ (eq. 8) as:

$$\Big(\mathbb{1}(X)\Big)_{\mathbb{V}_k} = \frac{1}{\text{card}(\mathbb{V}_k)} \left(\mathbb{1}_{\mathbb{V}_k}(s_1) \dots \mathbb{1}_{\mathbb{V}_k}(s_8)\right)_X \tag{9}$$

where the indicative function $\mathbb{1}_{\mathbb{V}_k}(s_i)$ is defined as

$$\mathbb{1}_{\mathbb{V}_k}(s_i) = \begin{cases} 1 \text{ if } s_i \in \mathbb{V}_k, \\ \\ 0 \text{ if not.} \end{cases} \tag{10}$$

We write the $n \times \dim(\mathbf{x}_{\mathbb{V}_k})$ transition matrix $\mathbf{\Phi}_{\mathbb{V}_k}$ as a block diagonal matrix:

$$\mathbf{\Phi}_{\mathbb{V}_k} = \begin{pmatrix} \Big(\mathbb{1}(X_1)\Big)_{\mathbb{V}_k} & 0 & \dots \\ 0 & \ddots & 0 \\ \vdots & 0 & \Big(\mathbb{1}(X_n)\Big)_{\mathbb{V}_k} \end{pmatrix} \tag{11}$$

The measurement equation of our system is written as follow:

$$\mathbf{y}_k = \mathbf{H}_k \mathbf{x}_k + \mathbf{v}_k \tag{12}$$

where $\mathbf{y}_k$ is the measurement vector of dimension n, $\mathbf{H}_k$ is a state-measurement matrix (identity matrix here) and $\mathbf{v}_k$ a measurement noise (white noise) with a covariance matrix $\mathbf{R}_k$.

A predictive filter consists in four steps [10]: i) the measurement of $\mathbf{y}_k$ and its uncertainty $\mathbf{R}_k$, ii) the calculation of the gain $\mathbf{K}_k$ (also called the Kalman gain), iii) the linear combination of the measurement and of the predicted state value, and finally iv) a projection ahead next site $k+1$. The following algorithm summarizes a recursive implementation of a predictive filter.

- Initialization

$(\mathbf{x}_{1|0}, \mathbf{S}_{1|0})$

ForEach k **do**

- Measurement

$(\mathbf{y}_k, \mathbf{R}_k)$

- Calculation of the gain

$$\mathbf{K}_k = \mathbf{S}_{k|\mathbb{V}_{k-1}} \mathbf{H}_k^T (\mathbf{H}_k \mathbf{S}_{k|\mathbb{V}_{k-1}} \mathbf{H}_k^T + \mathbf{R}_k)^{-1}$$

- Correction

$$\mathbf{x}_k = \mathbf{x}_{k|\mathbb{V}_{k-1}} + \mathbf{K}_k (\mathbf{y}_k - \mathbf{H}_k \mathbf{x}_{k|\mathbb{V}_{k-1}})$$

$$\mathbf{S}_k = (\mathbf{I} - \mathbf{K}_k \mathbf{H}_k) \mathbf{S}_{k|\mathbb{V}_{k-1}}$$

- Prediction

$$\mathbf{x}_{k+1|\mathbb{V}_k} = \mathbf{\Phi}_{\mathbb{V}_k} \mathbf{x}_{\mathbb{V}_k} + \mathbf{w}_k$$

$$\mathbf{S}_{k+1|\mathbb{V}_k} = \mathbf{\Phi}_{\mathbb{V}_k} \mathbf{S}_k \mathbf{\Phi}_{\mathbb{V}_k}^T + \mathbf{Q}_k$$

Recursive implementation of a predictive filter for DTM generation.

3.2 Estimating the local slope

The terrain height estimation depends both on the local slope and on the local neighbourhood ($\mathcal{V}_s$) extension of a site s. Figure 6 (top) shows the difference between two DTMs calculated with and without the integration of the local slope and a profile (bottom) of a DTM (0.5 m resolution) integrating the computation of the local slope. If altimetric discrepancies are negligible over flat areas, they are particularly high over the most sloppy areas where discrepancies can reach 2.5 m.

The quality of the local plane estimation depends on the lidar point geostatistics within $\mathcal{V}_s$ and defines the terrain height relevancy as well as its uncertainty. We estimate a plane $n_x x + n_y y + n_z z + d = 0$ with $(n_x, n_y, n_z) \in [-1, 1]$ and $d \in \mathbb{R}$ from lidar points belonging to the first mode of the altimetric distribution of $\mathcal{V}_s$. The first mode contains the set of lidar points of lowest altitude that may belong to the terrain. It is the entire distribution if only one mode has been detected. The 3D plane estimation is then performed in the barycentric frame. A robust M-estimator has been used with a L_p-norm [11]. This algorithm is implemented as an iterative re-weighted least square system. The calculation of such a local tangent plane considering each site as independent of its local environment has shown incoherences between neighbouring planes. Figures 7 show the (n_x, n_y, n_z) components of the normal vectors calculated independently on each site. These components are noisy and make incoherences appear on the terrain topography. These side-effects can be overcome using the predictive filter paradigm to estimate the local slope that takes into account the local environment of each site. Using notations defined in section 3.1, $\mathbf{y}_k$ and $\mathbf{x}_k$ are vectors of dimension 4 , $\mathbf{x}_{\mathbb{V}_k}$ is a 32 component vector in case of a 3×3 neighbourhood and $\mathbf{\Phi}_{\mathbb{V}_k}$ is a 4×32 matrix. The measurement $\mathbf{y}_k$ is computed from the M-estimator. Here, $\mathbf{v}_k$ is a Gaussian white noise of zero mean

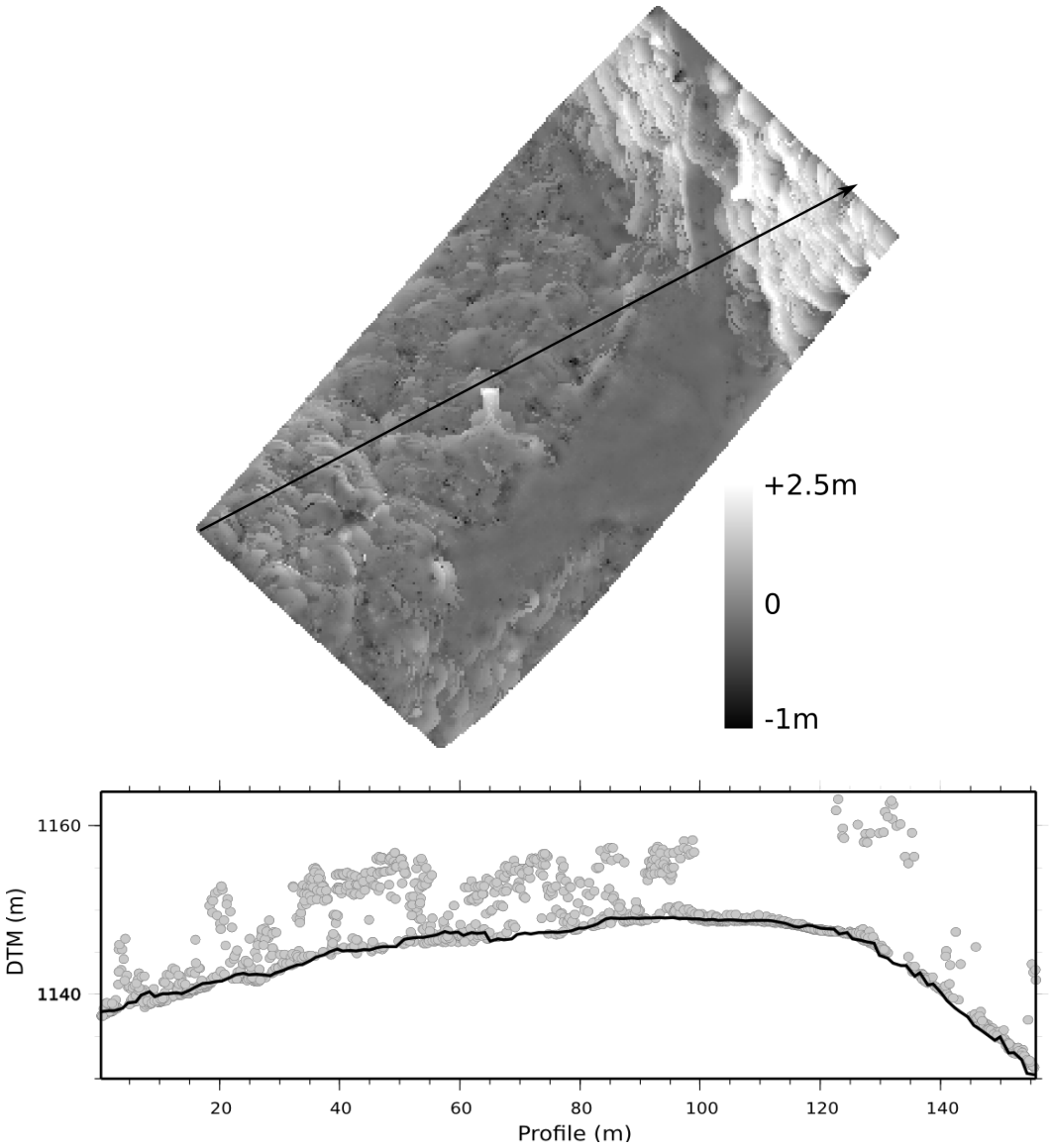

Fig. 6. **Top**: Altimetric difference between two DTMs computed with and without the integration of the local slope. Discrepancies are coded in a grey level scale from -1 m to 2.5 m. **Bottom**: Profile along the black arrow of the DTM calculated with the local slope. Grey points are lidar points.

and $\sigma^2 = 0.005$. The covariance matrix $\mathbf{R}_k$ of the slope "measurement" is a diagonal matrix corresponding to the 99% confidence interval around each parameter estimate [1] .

[1] For a linear system $AX = B$ where A is the design matrix, B the data and X the parameter vector, the covariance matrix of the estimate $\hat{X}$ can be written as $C = \sigma^2({}^tAA)^{-1}$. The

The prediction relation can be rewritten as:

$$\mathbf{x}_{k+1|\mathbb{V}_k} = \frac{1}{\text{card}(\mathbb{V}_k)} \sum_{s_i \in \mathbb{V}_k} \begin{pmatrix} n_x(s_i) \\ n_y(s_i) \\ n_z(s_i) \\ d(s_i) \end{pmatrix} \mathbb{1}_{\mathbb{V}_k}(s_i) \tag{13}$$

Figure 7 shows local normal vectors calculated on $0.5\,\text{m}$ resolution grid and displayed in grey level scale. The dynamic of images has been modified for display purposes. They shows the improvement of the normal vector calculation in all three coordinates in terms of regularity using a predictive filter with regard to a calculation performed independently on each site.

3.3 Estimating the terrain elevation

Again, the first mode of the altimetric distribution is extracted. We then project the lidar points belonging to the first mode into the local frame centred on site k and oriented following the local normal vector $(n_x, n_y, n_z)^T$ calculated previously. For a site k, we denote $\mathcal{F}_k$ the lidar point set belonging to the first mode and projected into the local frame. Because of the inhomogeneous spatial/planimetric distribution of lidar points as well as the high value of $\mathbf{d}_k$, the terrain height is interpolated using an *Inverse Distance Weighting* function.

$p\%$ confidence interval is written for each component of $\hat{X}$ as $x_j = \hat{x}_j \pm t(n-m, p\%)\sqrt{C_{jj}}$ where $t(n-m, p\%)$ is the value of the Student coefficient with $n-m$ d.o.f. at a level of confidence p.

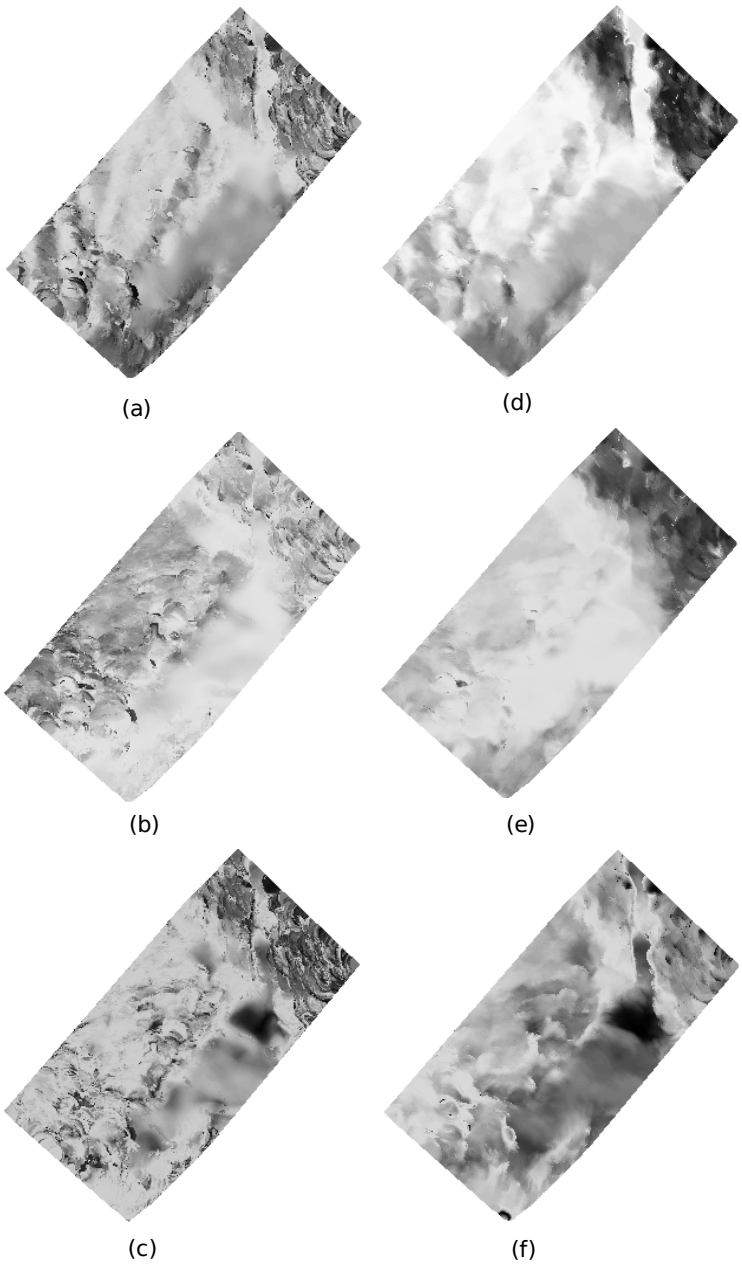

Fig. 7. Local normal vectors calculated on 0.5 m resolution grid and displayed in grey level scale. The dynamic of images has been modified for display purposes. (a), (b), (c) correspond to the three components calculated independently on each site. (d), (e), (f) correspond to the three components calculated using a predictive filter.

The uncertainty associated to the terrain height depends on the lidar point statistics of the first mode in the local frame $(n_x, n_y, n_z)^T$.

We consider the terrain estimate accurate at one standard deviation of the altimetric distribution of $\mathcal{F}_k$.

The predictive filter then manages the uncertainty propagation. Here, $\mathbf{v}_k$ is a Gaussian white noise of zero mean and $\sigma^2 = 0.01$, accuracy of the lidar system. Considering ξ_i as the inverse of the planimetric Euclidean distance between a site k and a lidar point $l_i \in \mathcal{F}_k$, we can write the following state equations for this system:

$$\mathbf{y}_k = \frac{1}{\sum_j \xi_j} \sum_i \xi_i \; z_{l_i} + \mathbf{v}_k \tag{14}$$

$$\mathbf{R}_k = \underset{\forall l_i \in \mathcal{F}_k}{\text{variance}} \left(z_{l_i} \right) \tag{15}$$

The predictive filter presented hereabove tends to smooth the terrain surface. Nevertheless, lidar points describe the topography with much more details, those interesting for a fine description of micro-relieves. The issue becomes a fusion problem where a coarse DTM has to incorporate 3D point information to become more precise but still regular. This problem can be modelled in a Bayesian framework [12].

4 Markovian regularization

4.1 Background

In a probabilistic framework, an image is a set S of sites s where the grey level is a descriptor of each site. An image is considered as a realisation of a random field $X = (X_s)_{s \in \mathbb{N}^2}$, where X_s is a random variable of values in $E^{card(S)}$ [13] . A random field is therefore a measurable mapping $X : \Omega \longrightarrow E^{card(S)}$ associated to a complete measurable space $(\Omega, \mathcal{F}, \mathbf{P})$. This model is described by the probability law $\mathbf{P}(X = x)$ the event x to be a realisation of X. As usual in image processing,

we will consider the particular Markov Random Fields (MRF). In a MRF, the value of a site only depends of its local environment through a neighbouring system $\mathbb{V}$ defined as [14]:

$$\begin{cases} s \notin \mathbb{V}(s) \\ \forall r \in S \backslash \{s\}, s \in \mathbb{V}(r) \Leftrightarrow r \in \mathbb{V}(s). \end{cases} \tag{16}$$

In case of a MRF, we have

$$\begin{aligned} \forall x \in \Omega, \forall s \in S, & \mathbf{P}(X_s = x_s | X_r = x_r, r \in S \backslash \{s\}) \\ & = \mathbf{P}(X_s = x_s | X_r = x_r, r \in \mathbb{V}_s) \end{aligned} \tag{17}$$

The Hammersley-Clifford theorem argues the equivalence between a MRF and a Gibbs field. The *a priori* probability of a random variable X can therefore be explicitly written as:

$$\mathbf{P}(X = x) = \frac{1}{Z} e^{-\mathcal{U}(x)} \tag{18}$$

where $Z = \sum_{x \in \Omega} e^{-\mathcal{U}(x)}$ is a normalization constant and $\mathcal{U}$ an energy function (which has the properties to be decomposed into local energies) defined as:

$$\begin{aligned} \mathcal{U} : \Omega & \longrightarrow \mathbb{R} \\ x & \longrightarrow \mathcal{U}(x) = \sum_{c \in \mathcal{C}} \mathcal{U}_c(x) \end{aligned} \tag{19}$$

We propose a Bayesian model for regularizing the terrain surface in order to introduce *a priori* knowledge on the model. The Bayes's law, which relates *a priori* and conditional probability is defined as

$$\mathbf{P}(X|D) = \frac{\mathbf{P}(D|X)\mathbf{P}(X)}{\mathbf{P}(D)} \propto \mathbf{P}(D|X)\mathbf{P}(X) \tag{20}$$

The Bayesian model is related to the inverse problem of how retrieving the best configuration $\hat{x}$ knowing observations D. We look for the maximum a posteriori

(MAP) defined as:

$$\hat{x}_{MAP} = \arg\max_{x \in \Omega} \mathbf{P}(X = x|D) \tag{21}$$

that can be written as

$$\hat{x}_{MAP} = \arg\min_{x \in \Omega} \Big(- log\Big(\mathbf{P}(D|X = x)\Big) - log\Big(\mathbf{P}(X = x)\Big)\Big) \tag{22}$$

Under the markovian hypothesis, solving equation 22 is equivalent to globally minimize an energy $\mathcal{E}$, sum of a data term $\mathcal{E}_d$ and of a regularization term $\mathcal{E}_r$, $\lambda \in \mathbb{R}$ is a weighting parameter

$$\hat{x}_{MAP} = \arg\min_{x \in \Omega} (\underbrace{\mathcal{E}_d + \lambda \mathcal{E}_r}_{\mathcal{E}}) \tag{23}$$

In our problem, $\hat{x}_{MAP}$ represents the optimal altitude of a site s.

4.2 Definition of the energy

4.2.1 The data term

The data term at site s depends on the Euclidean distance between the terrain height x_s and a value ζ_s considered as a surface attractor. We consider that lidar points located within a buffer zone over the initial DTM may contribute to a better description of the reality of the terrain surface. However, the predictive filter described previously generates a terrain surface but also a standard deviation σ_{x_s} associated to these measurements. Therefore, this buffer zone is defined for each site as proportional to the associated standard deviation. Based on the lidar point set $\mathcal{N}_s$ (square neighbourhood) bounded by the DTM resolution and within the tolerance layer at site s, ζ_s is finally calculated as the average altitude of lidar point belonging to $\mathcal{N}_s$. Besides, when no lidar points are detected within the tolerance layer, the Kalman surface is used. The Euclidean distance is then weightened by the number of lidar

points (card($\mathcal{N}_s$)) if there are any. It not, the weight ϖ is set to 1.

We define the set $D = \{s/ - q\sigma_{x_s} \leq x_s - \zeta_s \leq q\sigma_{x_s},\ q \in \mathbb{N}\}$. The Euclidean distance has to be minimal so that the final DTM should be as near as possible from laser measurements considered as the ground. We therefore define $\mathcal{E}_d$ as:

$$\mathcal{E}_d(D|X = x_s) = \varpi(\zeta_s - x_s)^2 \text{ with } \varpi = \max\left(1, \text{card}(\mathcal{N}_s/s \in D)\right) \tag{24}$$

4.2.2 The regularization term

The regularization term aims to compensate the effect of the data term so that the final surface should not be too noisy. This term depends on the intrinsic geometry of the surface [15].

Let h be the surface defined as:

$$\begin{aligned} h : \mathbb{R}^2 &\longrightarrow \mathbb{R}^3 \\ (x, y) &\longrightarrow (x, y, z = h(x, y)) \end{aligned}$$

A second order Taylor development at point $\mathbf{u_0} = (x_0, y_0)$ with $\mathbf{u} = [x\ y]^T$ can be written

$$\begin{aligned} h(\mathbf{u}) = &\underbrace{h(\mathbf{u_0}) + (\mathbf{u} - \mathbf{u_0}).\nabla_{\mathbf{u_0}} h}_{\Pi_0(\mathbf{u})} \\ &+ \frac{1}{2}(\mathbf{u} - \mathbf{u_0})\mathbf{H}(\mathbf{u} - \mathbf{u_0})^T + o(||(\mathbf{u} - \mathbf{u_0})||^2) \end{aligned} \tag{25}$$

where Π_0 is the tangent plane to h in $\mathbf{u_0}$ and $\mathbf{H} = \begin{pmatrix} \frac{\partial^2 h}{\partial x^2} & \frac{\partial^2 h}{\partial x \partial y} \\ \frac{\partial^2 h}{\partial x \partial y} & \frac{\partial^2 h}{\partial y^2} \end{pmatrix}$ the Hessian matrix of h. This matrix describes the local properties of the surface curvature.

We define the regularization term as a function of the trace and the determinant of the Hessian matrix. The trace describes the local convexity of the surface while the

determinant is linked to the shape of the surface with regard to its tangent plane (parabolic, elliptic, hyperbolic). We therefore define $\mathcal{E}_r$ as:

$$\mathcal{E}_r = \alpha_1 tr(H)^2 - \alpha_2 \text{det}(\mathbf{H}) \quad \alpha_1, \alpha_2 \in \mathbb{R}^+ \tag{26}$$

$$= \frac{\alpha_2}{2}\left(\left(\frac{\partial^2 h}{\partial x^2}\right)^2 + \left(\frac{\partial^2 h}{\partial y^2}\right)^2\right) + \alpha_2\left(\frac{\partial^2 h}{\partial x \partial y}\right)^2 + (\alpha_1 - \frac{\alpha_2}{2})\left(\frac{\partial^2 h}{\partial x^2} + \frac{\partial^2 h}{\partial y^2}\right)^2 \tag{27}$$

This energy is designed so that its convexity should be managed for optimization purposes. Indeed, in case of estimating a fine terrain surface, there are not any forbidden natural shapes. A repulsive term is therefore not appropriate. If the constrains

$$\alpha_2 \geq 0 \text{ and } \alpha_1 \geq \frac{\alpha_2}{2} \tag{28}$$

are applied, the energy becomes convex. In practice, $\alpha_1 = 1$ and $\alpha_2 = 1/2$.

4.2.3 Optimization

Since $\mathcal{E}$ is a separable energy in a Markovian formulation of the problem, the optimization is based on an Iterated Conditional Mode (ICM) algorithm [16]. It is split into subproblems, each of them applied to a particular DTM site (eq. 19). The related local energy at site s is denoted $\mathcal{E}_s$. An iteration toward the global minimum of $\mathcal{E}$ is denoted $\mathcal{E}^{\text{it}}$ in the following algorithm. Because of the convexity of $\mathcal{E}$, the minimum is locally found using a steepest gradient method with constant step δ. The following algorithm summarizes the optimization steps where index t refers to an iteration on a particular site toward the local minimum. The convergence is

obtained when the global energy has no significant changes within ϵ.

While $\left| \dfrac{\mathcal{E}^{\text{it}} - \mathcal{E}^{\text{it}-1}}{\mathcal{E}_{\text{min}}} \right| < \epsilon$ **do**

For Each site s

While $\mathcal{E}_s(x_s^t) < \mathcal{E}_s(x_s^{t-1})$ **do**

$x_s^t = x_s^{t-1} + \delta \, \text{sgn}\left(\mathcal{E}_s(x_s^t - \delta) - \mathcal{E}_s(z_s^t + \delta)\right)$

Details of the optimization step of the Markovian regularization.

5 Results and discussion

5.1 Review of the methodology

The input data consists of lidar data. In corresponding DTM topology, a landscape predictor mask based on variance allows to detect regions with off-ground points. This mask is used to adapt the local neighbouring system (section 2.3). The processed distance $\mathbf{d}_s$ is used in the following propagation along DTM sites. We assume that the terrain height is generally provided by the lowest points. For each site k, ground points are likely to belong to the first mode of the vertical distribution $\mathcal{V}_s$. Based on a predictive Kalman paradigm, the local slope is estimated for each site (section 3.2). A slope prediction is processed for the next site $k + 1$. The first mode is then projected into a local frame along the estimated plane. The terrain height is estimated based on the same predictive paradigm (section 3.3). The propagation along DTM sites provides a predictive DTM (or Kalman DTM) and the corresponding error measure σ_{DTM}. Both are used in the regularization step. The predictive DTM provides low frequency of the relief. The Markovian regularization (section 4) refines finally the height surface. The global methodology is reminded

as a workflow in figure 8 and a review of the parameters is presented in table 1.

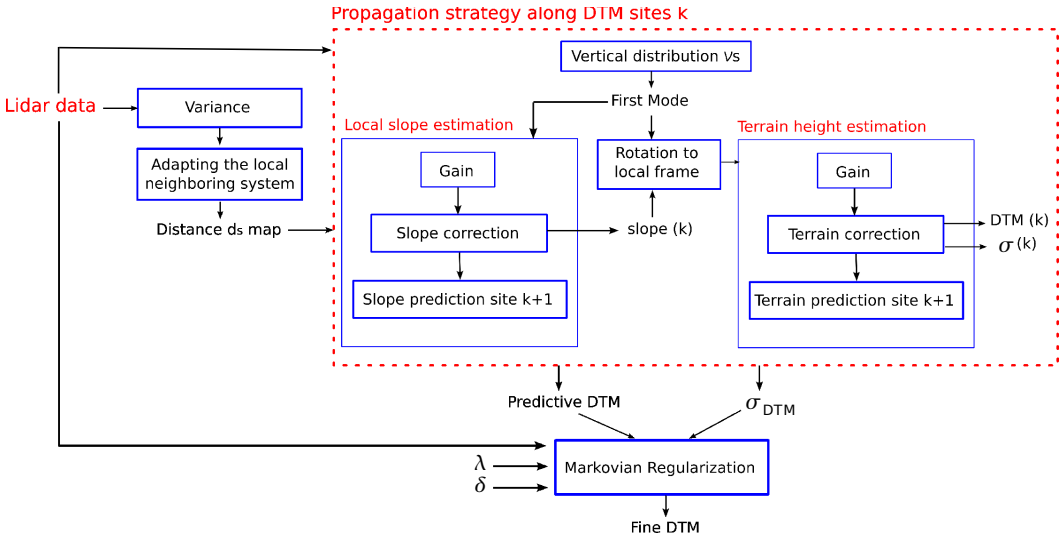

Fig. 8. Flowchart of the whole methodology.

5.2 The data set

The algorithm has been tested on a large data set over Le Brusquet in France. It is a mountainous area with steep relieves and vegetation. The whole data consists of 23.10^6 laser points. We present the results obtained from a 2.6km$\times$1.6km area subset of Le Brusquet's data (figure 9).

The data acquisition was performed in April 2007 using a RIEGL LMS-Q560 system. The lidar system operated at a pulse rate of 111 kHz. The flight height was around 500 m leading to a footprint size of about 0.25 m. The point density was about 5 pts$/m^2$. After filtering outliers, the point density is about 1.8 pts $/m^2$.

As mentioned in section 2.1, the entire survey is paved into lidar point subsets of roughly $1.5.10^6$ points (figure 1) with 40 m overlap. The DTM is processed independently on each subset. The entire final DTM is finally reconstructed by mosaicking the different DTMs.

Process	Parameter	Value
Variance	σ_{min}	1m
Adapting local neighboring system	$\mathbf{d}_{\text{min}}^{\text{abs}}$	auto
	d_s^{max}	$5d_s^{min}$
	c	6
	β	3
Vertical distribution	class width	0.3 m
Predictive Kalman paradigm	-	-
Markovian regularization	q (Buffer Zone)	6
	λ (regulariation parameter)	0.1 m
	δ (steepest gradient step)	0.01 m

Table 1

Review of the parameters

5.3 Results

Figure 10 shows the final DTM over the entire area of Le Brusquet using a 3D shaded bird's eye view. Small details like roads or microrelieves are clearly visible. Figure 11 is the textured DTM with the corresponding orthorectified aerial image. The mountain flanks are dark due to the sun shadow. Nevertheless, roads are particularly well reconstructed at the fore front.

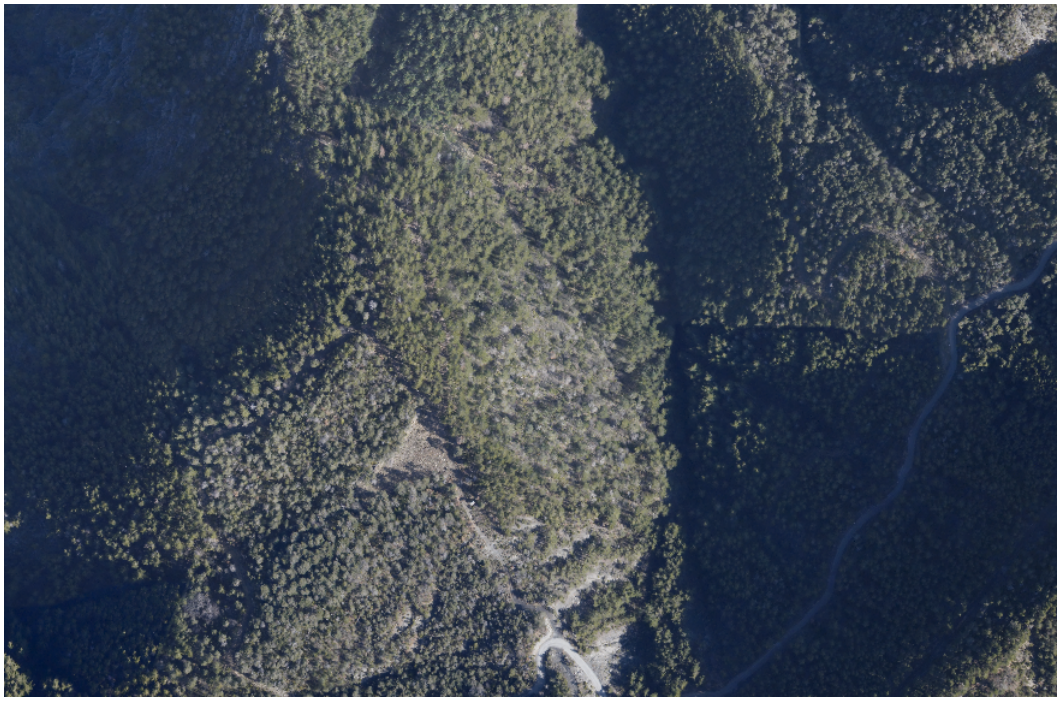

Fig. 9. Orthorectified image of the area wheron reuslts are presented.

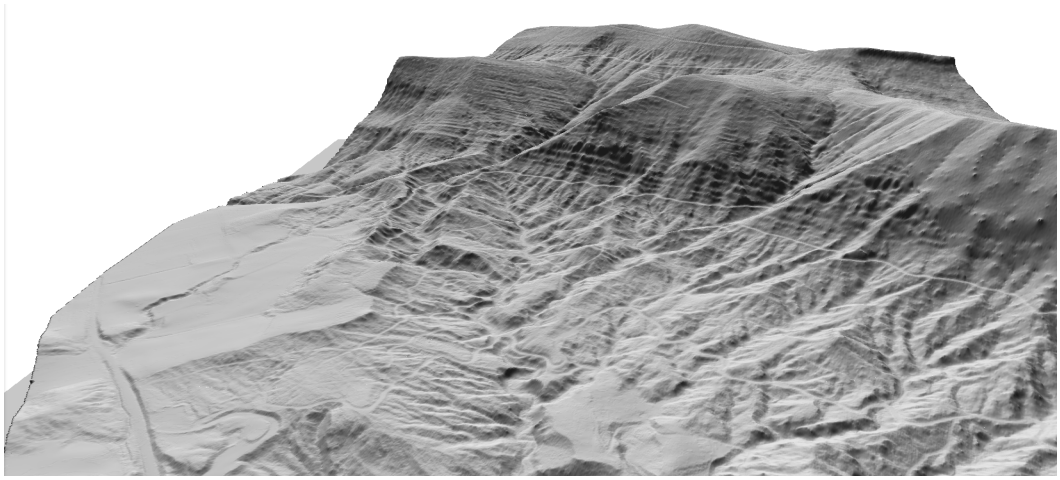

Fig. 10. 3D bird's eye view of a shaded DTM over Le Brusquet, France.

5.4 Discussion

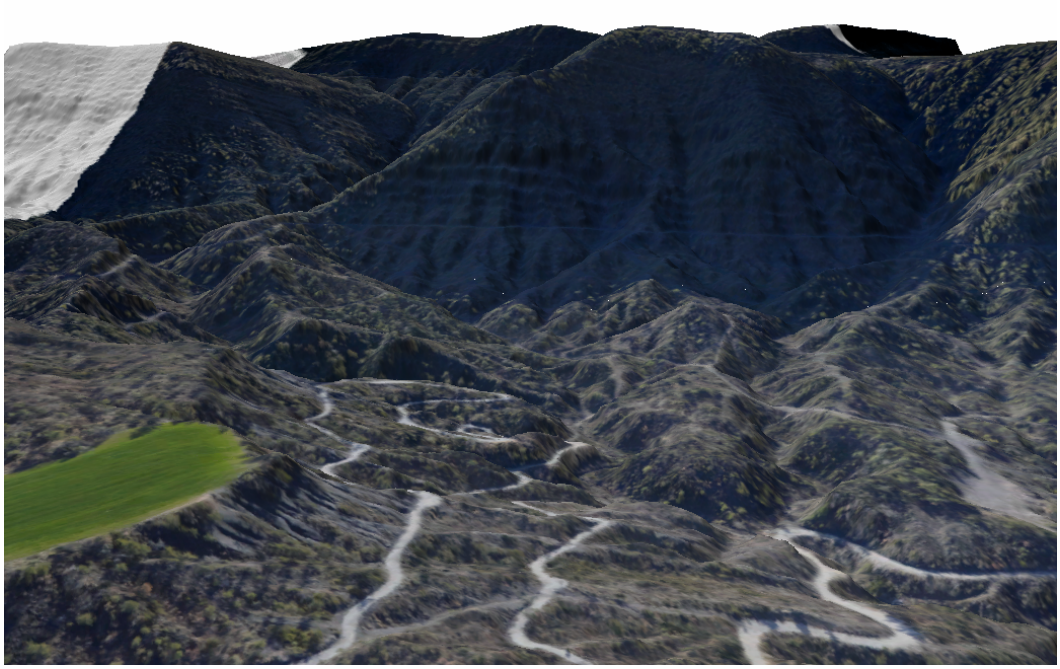

Fig. 11. 3D bird's eye view of the textured DTM over Le Brusquet, France. The texture image is the orthorectified image.

5.4.1 On the predictive filter

Figure 13 and 14 show two profiles of different outputs of the algorithm following a coherent x-axis. Regarding the local neighbourhood diameter $\mathbf{d}_s$, one can remark on both profiles that the diameter increases while lidar ground points are missing and is kept minimal while not. Figure 12 shows the values of $\mathbf{d}_s$ superimposed on the final DTM. We decided to manage a priori information before hand by generating a landscape predictor mask and to adapt the local environment depending on this predictor. If other predictors would be required (urban areas, watered areas ...), we would need to relate the geostatistics of lidar points to these predictors. The behaviour of the statistics of lidar data depending on the landscape has still to be investigated in terms of reflectivity and geometry.

Generally, in natural landscape and at a global scale, the probability of lidar pulses to be transmitted through the canopy cover is higher than their probability to be

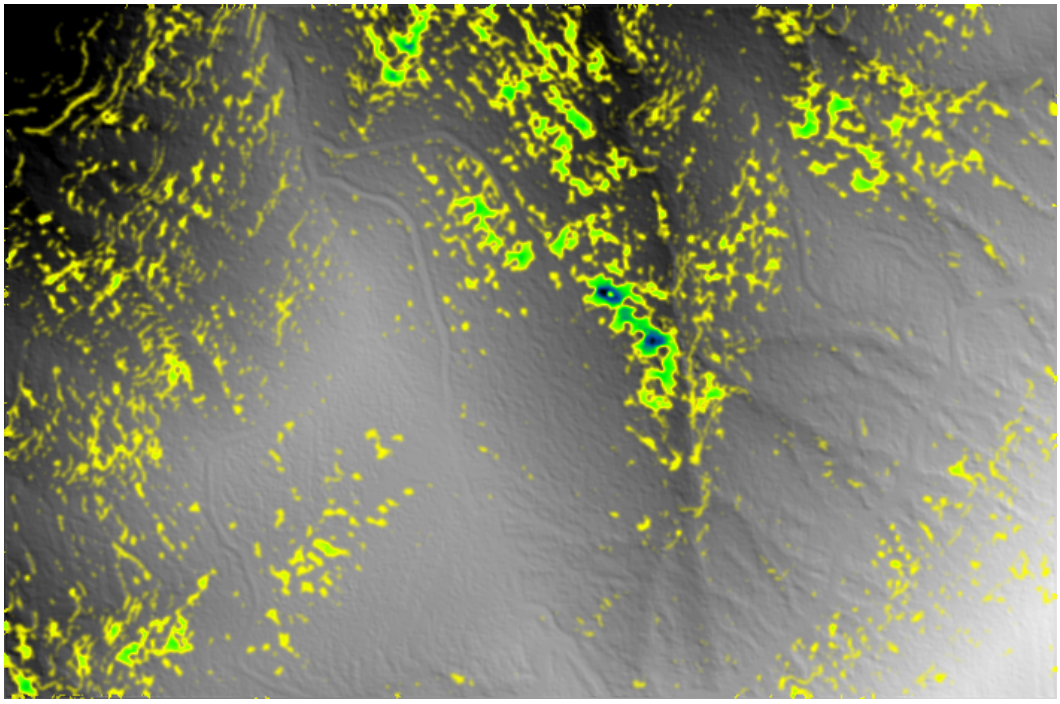

Fig. 12. Superimposition of $\mathbf{d}_s$ values and of the final DTM. $\mathbf{d}_s$ are presented in a color scale from low values (transparent and yellow) to medium (green) and highest values (dark blue).

reflected by the canopy top or by lower canopy level. Therefore, the first altimetric mode is likely to belong to the terrain and $\mathbf{d}_s$ is kept minimum. Thus, the terrain measurement and the prediction are almost similar at a global scale, which is well adapted for linearly combining both values. It is confirmed by the mean value of the Kalman gain along profile in figure 13 where $\overline{\mathbf{K}} = 0.5$. When $\mathbf{d}_s$ increases, i.e. when the probability of finding ground points increases, the terrain measurement is less accurate in case of relief and the surface is smoothed. The prediction is therefore privileged (e.g. $\mathbf{K}(75\,\mathrm{m}) = 0.13$ and $\mathbf{d}_s(75\,\mathrm{m}) = 35\,\mathrm{m}$).

The uncertainty associated to the DTM follows the opposite variations of the gain's ones. A high gain weights more the measured values with regard to the predicted one and enhances the DTM accuracy. This uncertainty varies around the variance of the white noise considered as the accuracy of the lidar measurement itself (sec-

tion 3.3). However, it is certainly under-estimated in terms of absolute accuracy. It should be improved with prior information. Using a multiple class landscape predictor/descriptor calculated from alternative data sources would improve our knowledge of the expected uncertainty. For instance, the density and the nature of the vegetation influences the penetration rate of a lidar beam within the canopy. In urban areas, buildings totally occlude the ground.

5.4.2 On the Markovian regularization

Results of the regularization step are presented on top profiles on figures 13 and 14. The improvement in terms of regularity is clearly visible. Figure 15 shows the image of the differences between the Kalman DTM and the regularized one. One can remark that the surface barely evolves when lidar points are considered as attractors (figure 16): the Kalman surface is well estimated when there are lidar ground points. Therefore, the data term over such sites is weightened in the energy minimization process by the number of lidar points. Figure 15 also shows that most of the deformations are positive (red pixels), i.e. that the regularized surface is higher that the Kalman surface. Indeed, the initial surface is meant to reproduce low frequencies of the terrain: in mountainous landscapes, crests and flanks can be under-estimated. More over, in case of dense vegetation, the algorithm increases $\mathbf{d}_s$ entailing an estimation of the terrain over a large area. As a result, the terrain is locally smoothed. If lidar attractors are located within the buffer zone (defined as proportional to the accuracy of the Kalman DTM), the surface will be strongly attracted, particularly along breaklines (crests, talwegs, path sides). Otherwise, within regions where there is no lidar points (transparent zones in figure 16), the surface will evolve mainly following the regularization term of the energy with the Kalman estimation as attractors. In a future work, we would like to integrate other a priori

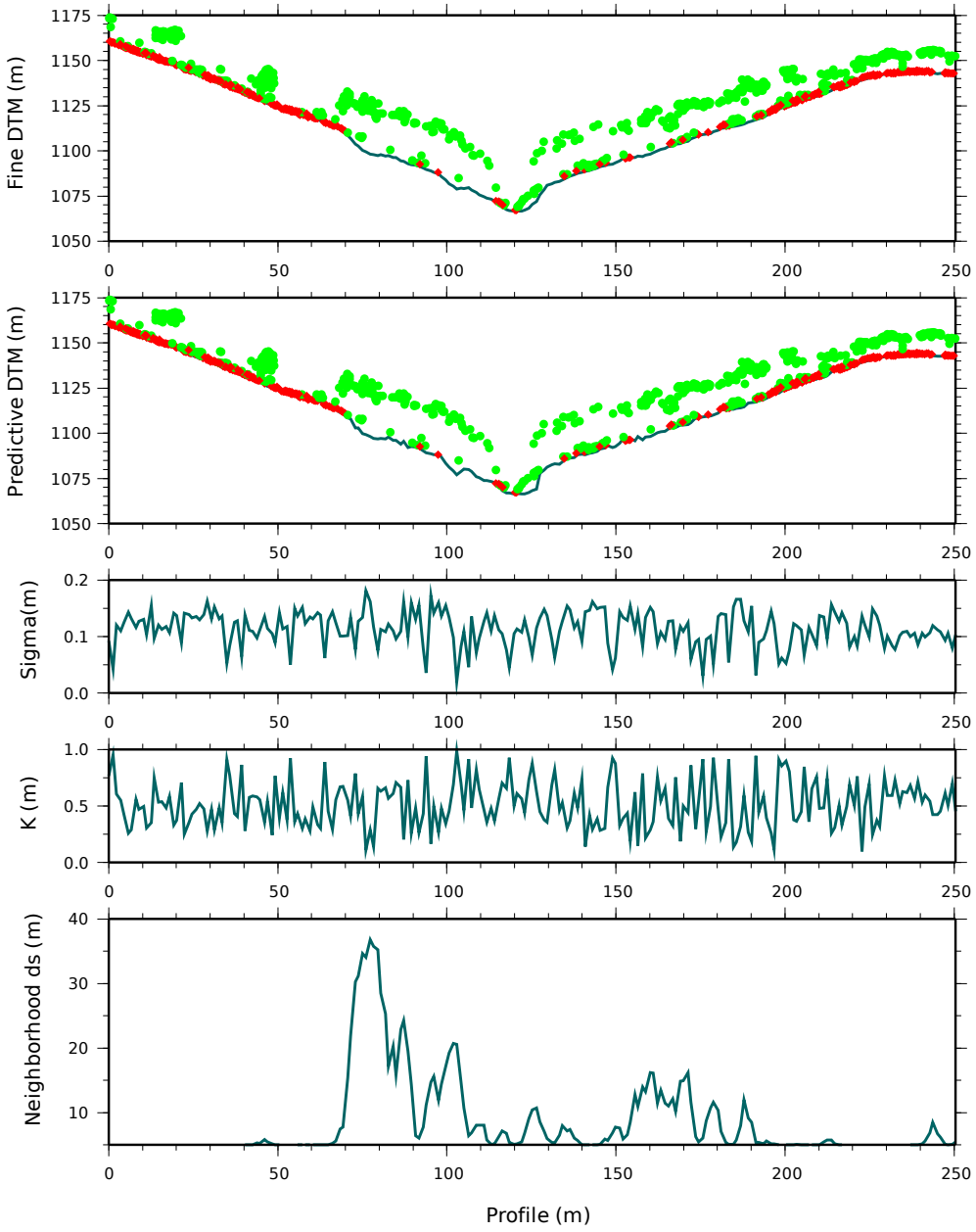

Fig. 13. Profiles of different outputs of the algorithm. From bottom to top: diameter of the cylinder used to estimate the terrain altitude in the Kalman filter, Kalman gain, standard deviation of the terrain heigh estimate, profile of the Kalman DTM and finally of the regularized DTM. In the last two plots, green points are lidar points considered to be off ground points while red diamonds are considered to be terrain points.

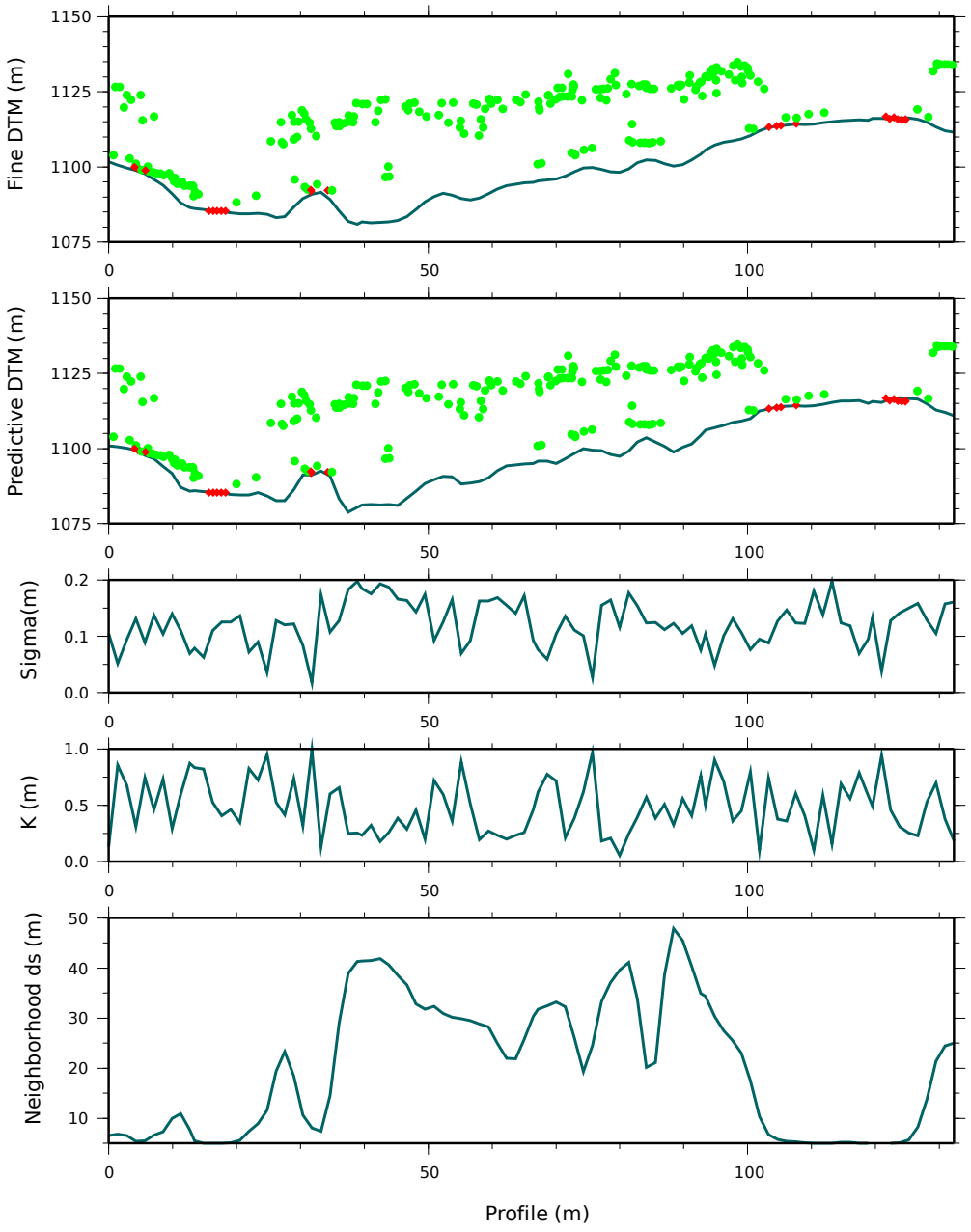

Fig. 14. Profiles of different outputs of the algorithm. From bottom to top: diameter of the cylinder used to estimate the terrain altitude in the Kalman filter, Kalman gain, standard deviation of the terrain heigh estimate, profile of the Kalman DTM and finally of the regularized DTM. In the last two plots, green points are lidar points considered to be off ground points while red diamonds are considered to be terrain points.

information like breaklines in the minimization process.

The algorithm is controled by two parameters: the weighting parameter of the regularization term λ and the step δ of the steepest gradient algorithm. No significant changes have been noticed when parameter λ belongs to $]0, 1]$. It is not a critical parameter in the algorithm because the data term is dominant most of the time. δ defines the final accuracy of the DTM. It is set to $\delta = 0.01\,m$. Nevertheless, as mentioned in section 5.4.3, there is no need to take a value smaller than the intrinsic accuracy of the lidar points.

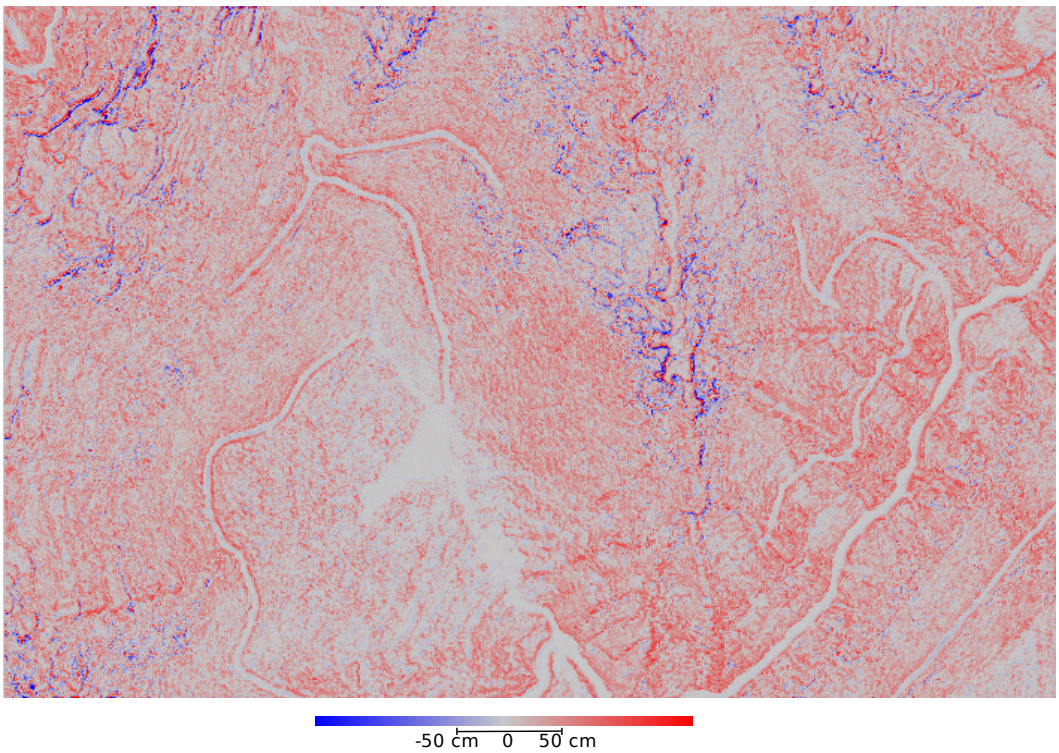

Fig. 15. Image of the differences between the Kalman DTM and the regularized one. The colour scale is set so that red colour represents positive displacements and blue colours negative displacements.

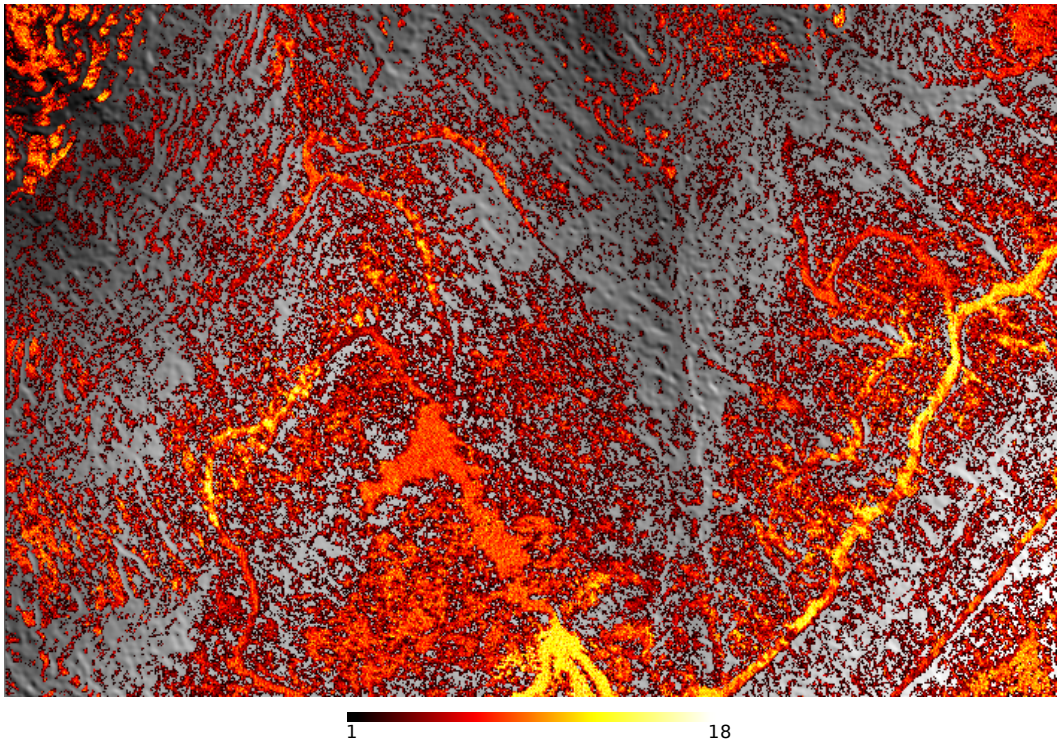

Fig. 16. Image of the number of attractors presented in a red hot color scale and superimposed to a shaded DTM.

5.4.3 Comparison with external data

In order to quantify the accuracy of the final DTM, external data have been acquired by the *** Institute *** using a terrestrial lidar. Such systems provide a centimetric accuracy along the lidar direction [17]. Figure 17 shows these terrestrial lidar points superimposed on the meshed DTM. We compared the distribution of the altimetric differences between terrestrial/airborne lidar points and the Kalman/regularized DTMs. Results are presented in figure 18 and in table 2. One can notice that the Kalman DTM is *on average* lower than both the airborne lidar points and the terrestrial lidar points (respectively -0.81 ± 0.7 m and -0.86 ± 0.63 m). As already mentioned, the Kalman filter is designed to be robust against outliers (estimation of the terrain over a large neighbourhood in case of high altimetric variance) and therefore may be underestimated to keep low frequencies of the terrain surface.

The distribution of the altimetric differences between the terrestrial/airborne lidar points and the regularized DTMs fully justify the regularization step: the average differences are respectively -0.16 ± 0.43 m and -0.16 ± 0.44 m. The intrinsic coherence of terrestrial/airborne lidar points in table 2 represents the average distance of lidar points with regard to a robust local plane. The intrinsic coherence can be observed in figure 19 where a "noise" clearly appear on airborne lidar points. After close investigations of the airborne point clouds, it appears that a mis-adjustment between two overlapping strips explains the higher intrinsic coherence of airborne lidar data.

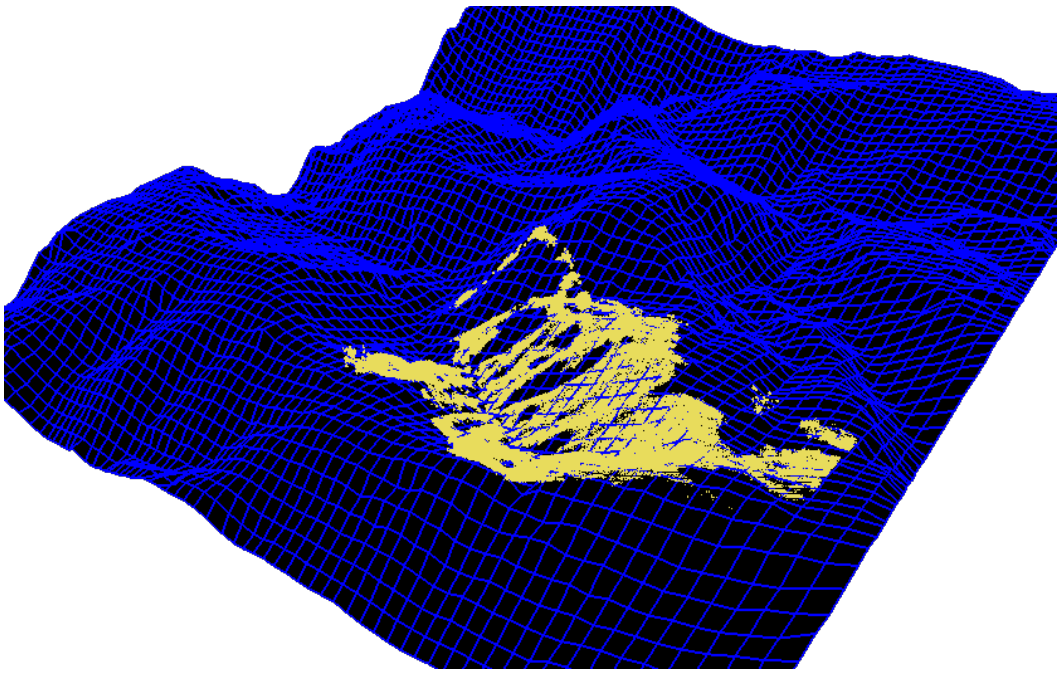

Fig. 17. Terrestrial lidar points (yellow points) superimposed on the meshed DTM.

6 Conclusion

We have presented in this paper a methodology for generating a Digital Terrain Model from 3D lidar data. It is a full operational system which works on complex and very large data sets. The main contribution of this work consists in using the

	Aerial Lidar points	Terrestrial Lidar points
Intrinsic coherence	$0.14\,\mathrm{m}$	$0.03\,\mathrm{m}$
Predictive DTM	$-0.81 \pm 0.7\,\mathrm{m}$	$-0.86 \pm 0.63\,\mathrm{m}$
Fine DTM	$-0.16 \pm 0.44\,\mathrm{m}$	$-0.16 \pm 0.43\,\mathrm{m}$

Table 2

Statistics of the DTMs with regard to terrestrial and airborne lidar points.

coherence of the terrain in a predictive filter paradigm to deal with the irregular point cloud representation of the topography. The predictive filter is designed to integrate both the local slope, and landscape predictors into the estimation of the ground altitude. The algorithm is based on few easy-tuned parameters.

In this paper, results are presented on mountainous landscapes with vegetation, but the methodology can be extended to different landscapes such as rural, urban and peri-urban areas provided that appropriate landscape predictors are available. Moreover, the improvement of the regularization process imposes the modelling and the integration of breaklines (crests, talwegs, mountain paths, building footprints, ...) in the global energy. Among other applications, the quality of the DTM manages the relevancy of the lidar point classification for studying off-ground features, but also ensures the quality of a reality-based landscape rendering for GIS-based applications.

References

[1] M. Pierrot-Deseilligny, N. Paparoditis, A multiresolution and optimization-based image matching approach: An application to surface reconstruction from SPOT5-HRS

stereo imagery, in: Proc. of the ISPRS Conference Topographic Mapping From Space (With Special Emphasis on Small Satellites), ISPRS, Ankara, Turkey, 2006.

[2] E. Ahokas, H. Kaartinen, J. Hyyppa, A quality assessment of airborne laser scanner data, in: Proc. of the ISPRS Workshop III/3 '3D Reconstruction from Airborne Laserscanner and InSAR' - International Archives of Photogrammetry and Remote Sensing, Vol. XXXIV, Dresden, Germany, 2003, pp. 1–7.

[3] G. Sithole, G. Vosselman, Experimental comparison of filter algorithms for bare-earth extraction from airborne laser scanning point clouds, ISPRS Journal of Photogrammetry and Remote Sensing 59 (1-2) (2004) 85–101.

[4] B. Petzold, P. Reiss, W. Stossel, Laser scanning - surveying and mapping agencies are using a new technique for the derivation of digital terrain models, ISPRS Journal of Photogrammetry and Remote Sensing 54 (1999) 95–104.

[5] W. Eckstein, O. Munkelt, Extracting objects from digital terrain models, in: Proc. Int. Society for Optical Engineering: Remote Sensing and Reconstruction for Three-Dimensional Objects and Scenes, Vol. 2572, 1995, pp. 43–51.

[6] K. Zhang, S.-C. Chen, D. Whitman, M. Shyu, J. Yan, C. Zhang, A progressive morphological filter for removing nonground measurements from airborne lidar data, IEEE Transactions on Geoscience and Remote Sensing 41 (4) (2003) 872–882.

[7] P. Axelsson, DEM generation from laser scanner data using adaptative TIN models, in: International Archives of Photogrammetry and Remote Sensing, Vol. XXXIII part B4/1, 2000, pp. 110–117.

[8] K. Kraus, N. Pfeifer, Determination of terrain models in wooded areas with airborne laser scanner data, ISPRS Journal of Photogrammetry and Remote Sensing 53 (1998) 193–203.

[9] F. Bretar, N. Chehata, Digital terrain model on vegetated areas: Joint use of airborne lidar data and optical images, in: Proc. of the ISPRS Conference Photogrammetric

Image Analysis (PIA), ISPRS, Munchen, Germany, 2007.

[10] G. Evensen, Data assimilation. The ensemble Kalman Filter, Springer, 2006.

[11] G. Xu, Z. Zhang, Epipolar Geometry in stereo, motion and object recognition, Kluwer Academic Publishers, 1996.

[12] F. Bretar, Processing fine digital terrain models by markovian regularization from 3D airborne lidar data, in: Proc. of the IEEE International Conference on Image Processing, San Antonio, U.S., 2007.

[13] P. Pérez, Markov random fields and images, Tech. Rep. 1196, INRIA (1998).

[14] S. Li, Markov random field modeling in computer vision, Springer Verlag, 1995.

[15] P. Fua, RADIUS: Image Understanding for Intelligence Imagery, Morgan Kaufmann, 1997, Ch. Model-Based Optimization: An Approach to Fast, Accurate, and Consistent Site Modeling from Imagery.

[16] J. Besag, On statistical analysis of dirty pictures, Journal of the Royal Statistical Society 48 (3) (1986) 259–302.

[17] A. Ruiz, W. Kornus, J. Talaya, J. Colomer, Terrain modeling in an extremely steep mountain: A combination of airborne and terrestrial lidar, in: Proc. of the XXth ISPRS Symposium, ISPRS, Istanbul, Turkey, 2004.

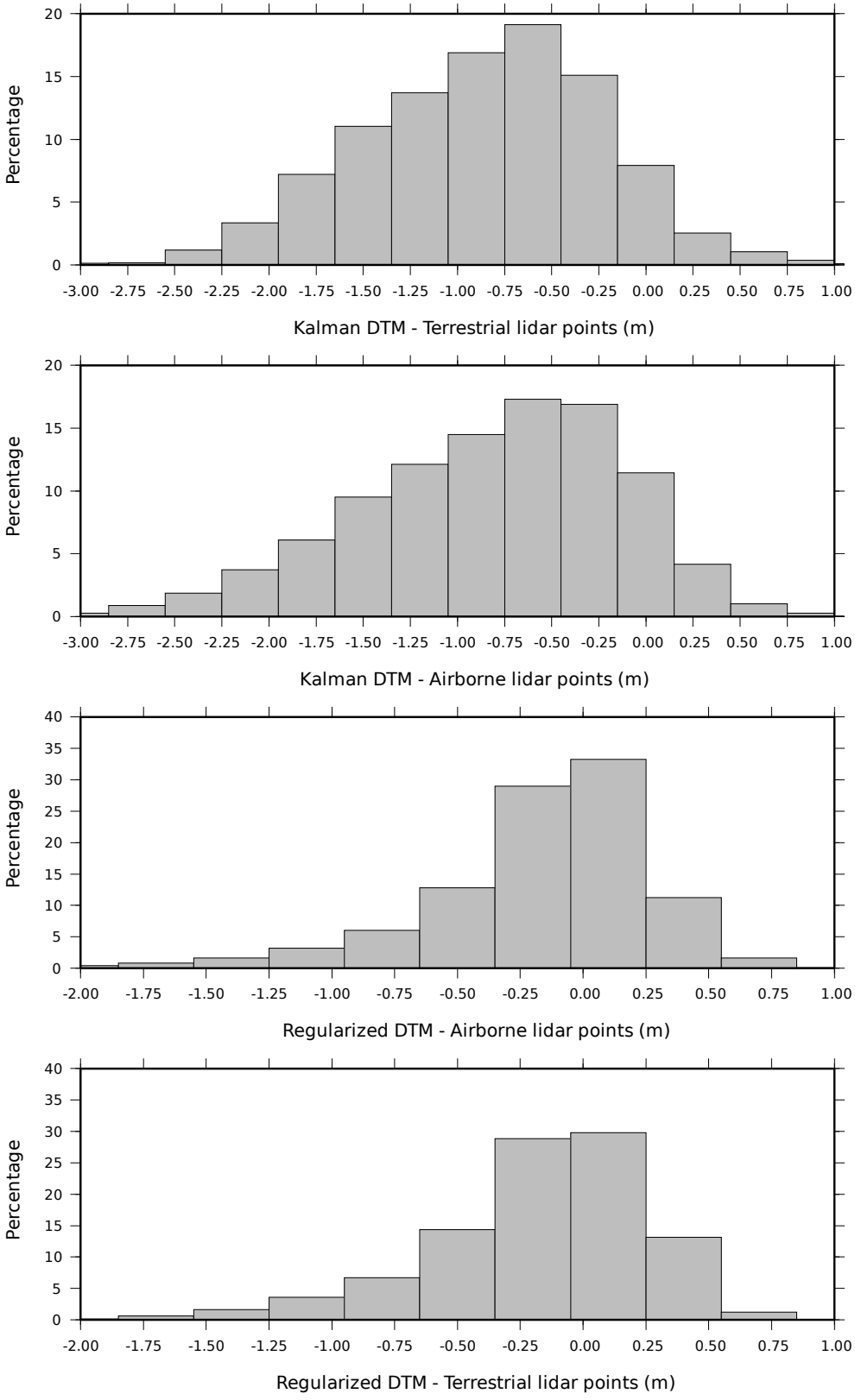

Fig. 18. Distributions of the altimetric differences between (from Top to bottom): Kalman DTM and terrestrial lidar, Kalman DTM and airborne lidar, regularized DTM and airborne lidar, regularized DTM and terrestrial lidar.

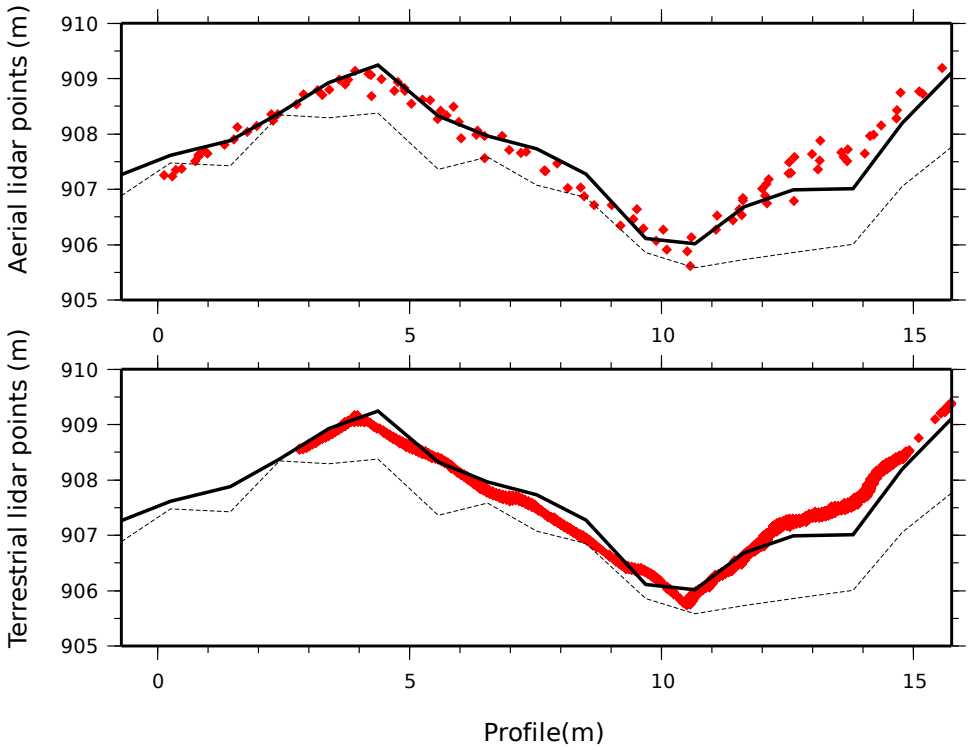

Fig. 19. Profiles of terrestrial and airborne lidar data (red points) as well as Kalman (dashed line) and regularized (black line) DTM.